Available online at www.keaipublishing.com/en/journals/journal-of-magnesium-and-alloys/

ScienceDirect

Journal of Magnesium and Alloys 13 (2025) 3642–3658

www.elsevier.com/locate/jma

Full Length Article

On the origin of non-basal texture in extruded Mg-RE alloys and its implication for texture engineering[☆]

X.Z. Jin[a,*], G.J. Yang[a], Xinyu Xu[d], D.B. Shan[a], B. Guo[a], B.B. He[c,*], C. Fan[b,*], W.C. Xu[a,*]

[a] National Key Laboratory for Precision Hot Processing of Metals & School of Materials Science and Engineering, Harbin Institute of Technology, Harbin, Heilongjiang 150001, China
[b] Zhejiang Institute of Modern Physics, School of Physics, Zhejiang University, Hang Zhou, Zhejiang 310058, China
[c] Department of Mechanical and Energy Engineering, Southern University of Science and Technology, Shenzhen, Guangdong 518055, China
[d] Department of Mechanical Engineering, The University of Hong Kong, Hong Kong 999077, China

Received 15 July 2024; received in revised form 22 August 2024; accepted 8 October 2024
Available online 12 November 2024

Abstract

The work aims to investigate the formation and transformation mechanism of non-basal texture in the extruded Mg alloys. With this purpose a pure Mg as reference and eight Mg-Gd binary alloys with the Gd concentration ranging from 0.5 wt.% to 18 wt.% were prepared for extrusion. This study shows that the basal fiber texture in pure Mg transited into RE (rare earth) texture in diluted Mg-Gd alloys and into the abnormal C-texture in high-concentration Mg-Gd alloys. In pure Mg, discontinuous dynamic recrystallization plays a predominant role during the extrusion process, resulting in the formation of a typical basal fiber texture. Alloying with high concentration of Gd impedes the dynamic recrystallization process, facilitating the heterogeneous nucleation of shear bands as well as the dynamic recrystallization within shear bands. Dynamic recrystallized grains within shear bands nucleate with a similar orientation to the host deformed parent grains and gradually tilt their c-axis to the extrusion direction during growth by absorbing dislocations, leading to the formation of either the RE-texture orientation or the C-texture orientation, depending on the stored energy within shear bands. The analysis aided by IGMA and TEM characterization reveals that the shear bands originate from the extensive but heterogeneous activation of pyramidal I slip. Tensile tests illustrate a close correlation between the fracture elongation and texture types. A comprehensive understanding of the formation and transformation mechanism of different texture components in Mg alloys holds significant importance for the design of high-performance Mg alloys by texture engineering.

Keywords: Mg alloys; Dynamic recrystallization; Shear bands; Pyramidal I slip; Texture engineering.

1. Introduction

As the typical light metals with a high specific strength, wrought magnesium (Mg) alloys have great potential for achieving excellent energy efficiency [1–3]. However, their applications in industries are limited by their poor plasticity/formability, mechanical anisotropy, and significant tension-compression yield asymmetry [4–6]. These drawbacks of wrought Mg alloys mainly result from the strong crystallographic texture, which are formed during the thermo-mechanical processing due to the limited activation of deformation modes. Unfortunately, the strong crystallographic texture cannot be effectively weakened or removed by annealing treatment afterwards [7]. For instance, a typical $<10\bar{1}0>$//ED (extrusion direction) basal fiber texture that develops after extrusion in pure Mg and conventional Mg alloys (e.g. AZ31 Mg alloy) undergoes subsequent transform into *a* $<11\bar{2}0>$//ED basal fiber texture or $<10\bar{1}0>$-$<11\bar{2}0>$ double fiber texture, which is characterized by a comparable

---

[☆] Peer review under the responsibility of Chongqing University.

[*] Corresponding author at: National Key Laboratory for Precision Hot Processing of Metals & School of Materials Science and Engineering, Harbin Institute of Technology, Harbin, Heilongjiang 150001, China.

E-mail addresses: jinxzabc@163.com (X.Z. Jin), hebb@sustech.edu.cn (B.B. He), cuncaifan@gmail.com (C. Fan), xuwc_76@hit.edu.cn (W.C. Xu).

https://doi.org/10.1016/j.jma.2024.10.004

intensity along with the occurrence of dynamic recrystallization [8].

To alleviate the texture effect in Mg alloys and improve their plasticity/formability, tremendous efforts have been undertaken, primarily by modifying their chemical compositions with rare earth (RE) elements [9,10], or by the use of special processing methods, such as asymmetric extrusion [11–13]. In particular, the alloying method has proven to be more effective for two primary reasons. Firstly, RE elements with a larger atomic radius tend to substitute the atoms on the basal plane of Mg alloys, thus leading to stronger solute-basal dislocation interactions [14]. Moreover, they can effectively increase the critical resolved shear stress (CRSS) of tension twinning by inhibiting the atomic shuffling process [15]. With the reduced CRSS ratio of non-basal dislocations to basal dislocations and non-basal dislocations to tensile twins, the activation of non-basal dislocations at room temperature or at high temperature will be enhanced [16]. Secondly, the addition of RE elements could decrease the I_1 stacking faults energy (SFE) of Mg alloys, thereby promoting the operation of <c + a> slip systems by increasing their heterogeneous source [5,17–20]. Consequently, the texture effect in the wrought Mg-RE alloys is weakened, as more profuse non-basal slip systems can be activated.

Instead of the sharp basal texture usually developed in pure Mg, a special texture component with $<11\bar{2}1>$ parallel to the extrusion direction (RE-texture) is often formed in the Mg-RE alloys after uniaxial extrusion. To rationalize such texture modification, numerous mechanisms have been proposed over the past two decades, including preferential nucleation at special sites [21,22], preferential growth of oriented grains [23–25], the increased activation of <c + a> dislocations [16] and solid solutes drag effect [26,27]. Recently, another texture component was also reported in Mg-RE alloys. The new component is termed as C-textured, as it is comprised of grains with c-axis preferentially aligned with the extrusion direction [28–31]. The formation mechanism of C-texture is, however, yet to be fully revealed. Moreover, the following questions also emerge with the appearance of the abnormal C-texture: (i) What is the selection mechanism between basal fiber texture, RE-texture and abnormal C-texture? (ii) How do the RE concentration and processing variables affect the texture evolution? (iii) Can we tailor the extrusion texture of a Mg-RE alloy by manipulating the processing variables? The responses to these inquiries establish the groundwork for enhancing the plasticity of magnesium alloys through texture engineering.

This work aims to investigate the dependency of extrusion texture with RE concentration and processing variables, to unravel the formation mechanism of different texture components in Mg-RE alloys, and finally to propose the strategies of tailoring extrusion texture of Mg-RE alloys. To achieve the aims, binary Mg-Gd alloys, in which the basal fiber texture [32], the RE-texture [32] and C-texture [30] are all reported, with a wide range of Gd content from 0.5 wt.% to 18 wt.% were prepared. In addition, an interrupted extrusion experiment combined with systematic electron backscattered diffraction (EBSD) measurements were conducted. To track the effect of different slip systems on texture evolution, the intergranular misorientation analysis (IGMA) technique and TEM characterization were conducted. The results provided clear evidence for understanding the formation mechanism of all kinds of extrusion textures in Mg alloys, which is of great significance for designing high-performance Mg-RE alloys with tailored mechanical properties.

2. Experimental procedure

The materials investigated in this study include a reference sample of pure Mg and eight Mg-Gd binary alloys with different Gd concentrations increasing from 0.5 wt.% to 18 wt.% (0.5 wt.%, 1 wt.%, 3 wt.%, 6 wt.%, 9 wt.%, 12 wt.%, 15 wt.% and 18 wt.%, respectively). Rods of pure Mg and Mg-Gd binary alloys, approximately 100 mm in diameter and 200 mm in length, were prepared by semi-continuous casting under the CO_2/SF_6 (100:1) protective atmosphere using pure Mg and pure Gd elements. In order to eliminate the effect of secondary phases in the as-cast Mg-Gd alloys, the rods of Mg-(0.5-6) wt.%Gd alloys were solid solution treated at 480 °C for 15 h, while the rods of Mg-(9-18) wt.%Gd alloys were treated at a higher temperature of 510 °C for 15 h. After the solid solution treatment, slabs (50 mm in diameter and 30 mm thick) were machined for extrusion. First, direct extrusion was conducted at 350 °C with an extrusion ratio of 25 at a ram speed of 3 mm/s for all alloys, forming a round bar with 10 mm in diameter, to reveal the effect of Gd concentration on the extrusion texture. Besides, an extra interrupted extrusion experiment, where the punch only moved down to a distance of 10 mm, was conducted both for the pure Mg and Mg-18Gd binary alloy to investigate the microstructure evolution with strain inside extrusion die. Finally, extrusion experiments under the other conditions, at 350 °C with an extrusion ratio of 9 and at 400 °C and 500 °C with an extrusion ratio of 25 alloy were also conducted for Mg-12Gd binary to explore the possibility of tailoring extrusion texture of Mg-Gd alloys. The corresponding alloy compositions and the designation of extrusion experiments are shown in Table 1.

The microtexture of as-extruded samples was characterized by EBSD in a dual beam focused ion beam field emission gun scanning electron microscope (FEI Helios NanoLab DualBeam 600i) equipped with an HKL EBSD detector, a CCD camera, as well as the data acquisition and analysis software packages. The EBSD data were acquired on the cross-section parallel with the extrusion direction (ED) of extruded bars using a voltage of 30 kV, a beam current of 3.2 nA, and a step size ranging from 0.2 μm to 0.5 μm depending on the grain size. Transmission electron microscopy (TEM) characterization was performed on a FEI Talos F200x transmission electron microscope with the operation voltage of 200 kV. The samples used for EBSD examination were prepared by a stepwise procedure: a first standard mechanical grinding using SiC paper with an increasing finer grit size, a subsequent mechanical polishing using diamond paste with the size from

Table 1
Alloy composition and extrusion parameters in this study.

Alloy designation	Reference	Mg-xGd alloy (wt.%)							
	Pure Mg	0.5	1	3	6	9	12	15	18
Direct extrusion (Temperature/Ratio)	350 °C/25	350 °C/25	350 °C/25	350 °C/25	350 °C/25	350 °C/25	350 °C/9 350 °C/25 400 °C/25 500 °C/25	350 °C/25	350 °C/25
Interrupted extrusion (Temperature/Ratio)	350 °C/25								350 °C/25

3 μm to 0.25 μm, and the final surface finishing using a colloidal silica suspension. The lamella for TEM characterization was prepared using a FIB trenching-and-lift-out technique. The average grain size was calculated based on the average line intercept obtained from the EBSD data by multiplying a shape factor of 1.74. Intragranular misorientation axis (IGMA) was analyzed to investigate the activation of different slip systems.

3. Results

3.1. Effect of Gd-concentration on the microstructure and microtexture of pure Mg and Mg-Gd binary alloy

Fig. 1 complies the EBSD inverse pole figure (IPF) orientation maps in the extrusion direction (ED) of pure Mg and Mg-Gd binary alloys after extrusion at 350 °C with an extrusion ratio of 25. It is clear that most of the specimens have been fully recrystallized with homogeneously equiaxed grains. Only two of the Mg-Gd binary alloys contain a small number of elongated grains, as demonstrated in Figs. 1(e) and (f). The average size of dynamically recrystallized grains for each alloy is plotted in Fig. 1(j). The variation of recrystallized grain size with the Gd concentration demonstrates that Gd alloying is highly effective in refining the microstructure of extruded Mg alloys. As expected, the extruded pure Mg possesses a larger average grain size, ~50 μm. By comparison, the average grain size of the extruded Mg-Gd binary alloys reduces to 15 μm when 0.5 wt.% Gd is added. It reduces slightly to 13 μm at 1.0 wt.% Gd, but then the average grain size levels off with increasing Gd concentration.

The effect of Gd concentration on the texture development can be demonstrated by the corresponding inverse pole figures in Fig. 2. As shown in Fig. 2(a), the extrusion of pure Mg at 350 °C establishes a typical basal fiber texture, composed of grains with the crystallographic orientation located along the $<10\bar{1}0>$-$<11\bar{2}0>$ boundary of unit triangle parallel with ED. As a consequence of complete dynamic recrystallization and apparent grain growth, the texture of extruded pure Mg is not as strong as the cold-deformed Mg alloys [33], only ~3.5 MRD (multiples of random distribution) in intensity. Minor alloying with Gd (~0.5 wt.%) has a slight effect on the extrusion texture component of Mg alloys, which is in agreement with earlier studies that texture modification occurs only when the Gd concentration exceeds a threshold limit [34,35]. In the Mg-0.5Gd alloy (Fig. 2(b)), the $<10\bar{1}0>$-axis fiber texture was preserved after extrusion, while the $<a>$-axis fiber texture component was weakened along with these corresponding grains tilting their c-axis a few degrees (~17.1°) toward the ED. Increasing the Gd concentration leads to a progressive rotation of the maximum texture pole from the $<10\bar{1}0>$-$<11\bar{2}0>$ boundary of unit triangle toward (0001) pole (the tilting angle increases from 17° to 40°), and finally stablishing a fairly strong single-pole $<11\bar{2}3>$//ED RE-texture with an intensity of 2.0 MRD in the Mg-9Gd alloy (Fig. 2(f)) after the intermediate configuration with arc distribution (Figs. 2(d) and (e)). The variation in the location of maximum texture pole with Gd concentration illustrates that the RE texture does not have a specific orientation but covers a wide crystallographic orientation range spanning from $<11\bar{2}0>$-$<10\bar{1}0>$ arc to (0001) pole in the stereographic triangle, which is also highly composition-dependent. Further increasing the Gd concentration up to 12 wt.% yields a bi-pole crystallographic texture in the Mg-Gd binary alloy (see Fig. 2(g)); one component is the RE texture with $<11\bar{2}3>$//ED, and the other is the abnormal C-texture, comprising grains with the c-axis aligned closely with the ED. Moreover, the color gradient between $(11\bar{2}3)$ and (0001) pole in the inverse pole figure of Mg-12Gd binary alloy provides the evidence that a higher proportion of grains are oriented between $<11\bar{2}3>$//ED and $<0001>$//ED compared with the Mg-Gd binary alloys with a lower Gd concentration. This indicates that the transformation from RE texture to C-texture is also a progressive rotation process. It is worth noting that the intensity of abnormal C-texture component increases sharply in the Mg-Gd binary alloys when the Gd concentration exceeds 12 wt.% (see Figs. 2(h) and (i)). When the Gd concentration increases up to 15 wt.% and 18 wt.%, the intensity of abnormal C-texture component reaches to 7.5 MRD and 15.4 MRD, respectively, which is comparable with the texture intensity of cold-rolled Mg alloys [33,36,37].

In summary, EBSD results reveal that a threshold concentration of Gd is required to trigger the formation of the RE texture and the abnormal C-texture. Moreover, the evolution from the basal fiber texture in pure Mg to the RE texture in dilute Mg-Gd alloys, and subsequently to the abnormal C-texture in high-concentration Mg-Gd alloys is not an abrupt event. Instead, it represents a Gd-concentration-dependent and progressive grain rotation process.

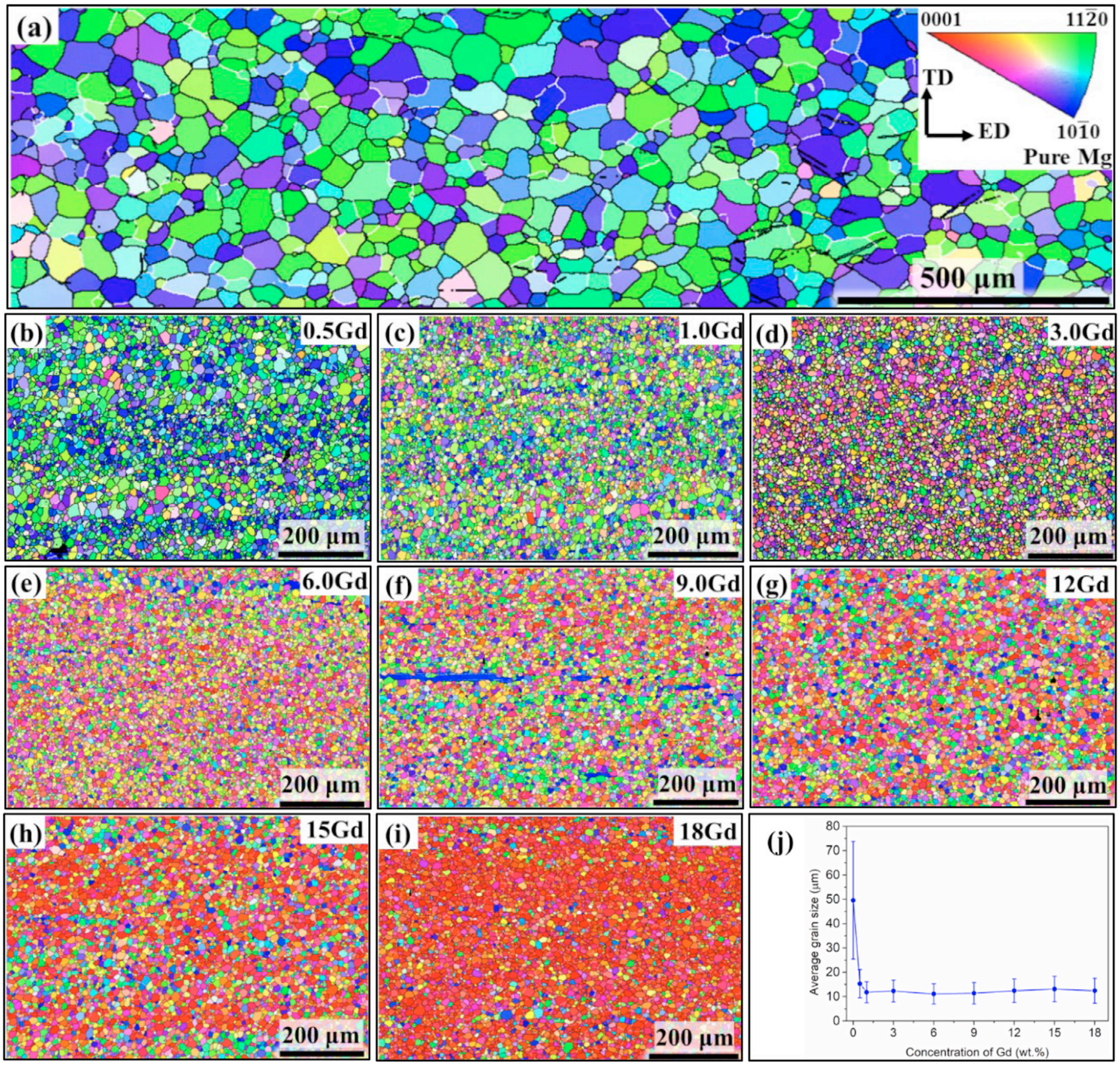

Fig. 1. IPF orientation maps (a-i) in the extrusion direction (ED) of samples extruded at 350 °C with an extrusion ratio of 25 and the corresponding average grain size (j): (a) pure Mg, (b) Mg-0.5Gd, (c) Mg-1Gd, (d) Mg-3Gd, (e) Mg-6Gd, (f) Mg-9Gd, (g) Mg-12Gd, (h) Mg-15Gd, (i) Mg-18Gd, (j) the variation of average grain size with the Gd concentration. The Gd concentration was also included as an insert in each figure.

3.2. Effect of extrusion parameters on the microstructure and microtexture of Mg-12Gd alloy

Fig. 3 presents the IPF orientation maps of Mg-12Gd alloy extruded under different conditions. The corresponding average grain size of dynamically recrystallized microstructure was also included as an inset in each figure. Extrusion at 350 °C with a ratio of 9 only activated the incomplete dynamic recrystallization in the Mg-12Gd alloy owing to the relatively small extrusion strain (Fig. 3(a)). Moreover, the average size of dynamically recrystallized grains was much smaller (only ~9.0 µm) compared with the Mg-12Gd alloy extruded at 350 °C with a ratio of 25 (~12.4 µm, Fig. 3(b)). With the increase of extrusion temperature, the average size of dynamically recrystallized grains of Mg-12Gd alloy increased progressively. When the extrusion temperature increased up to 400 °C and 500 °C, the average size of dynamically recrystallized grains increased up to 18.8 µm and 38.2 µm, respectively, as shown in Figs. 3(c) and (d).

As illustrated by the inverse pole figures in Figs. 4(a)-(b), after extrusion at 350 °C, the Mg-12Gd alloy possesses a bipole texture, consisting of RE texture and abnormal C-texture. However, in comparison with the Mg-12Gd alloy extruded at 350 °C with a ratio of 25 (Fig. 4(b)), the intensity of RE texture increased slightly along with the weakening of C-texture in the Mg-12Gd alloy after extrusion with a smaller ratio of 9 (see Fig. 4(a)). Increasing the extrusion temperature to 400 °C has little effect on the intensity of C-texture but established a weak basal texture by consuming the RE texture in the Mg-12Gd alloy extruded with a ratio of 25 (Fig. 4(c)). Further increasing the extrusion temperature to 500 °C, at which

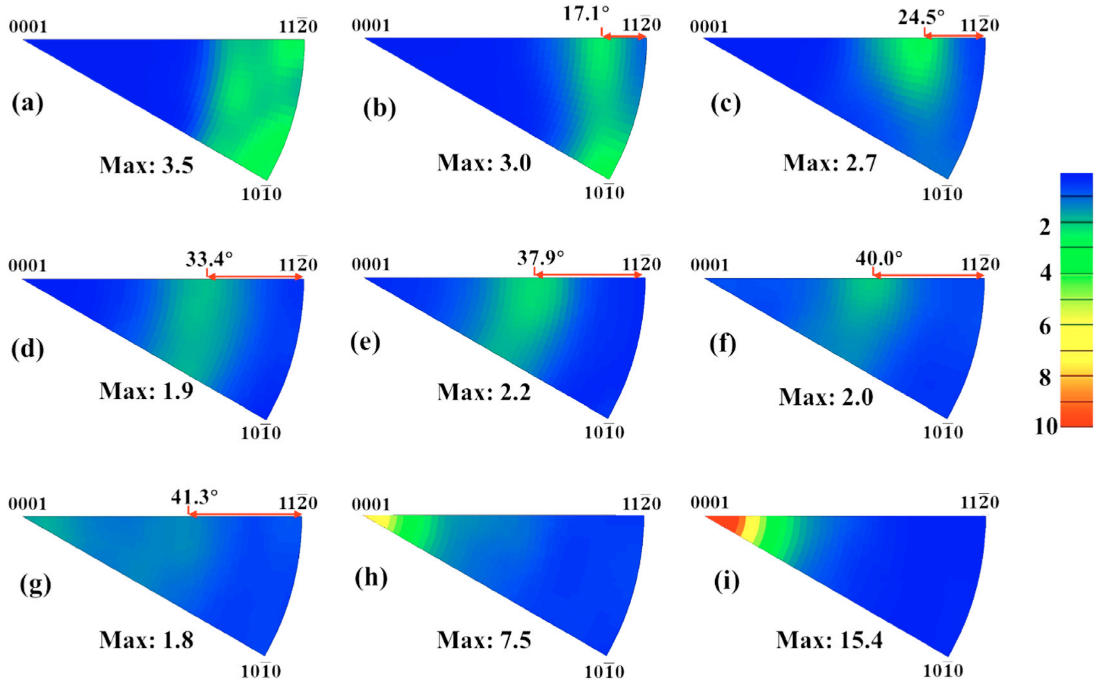

Fig. 2. Inverse pole figures (in the ED) of the recrystallized microstructure in samples extruded at 350 °C with an extrusion ratio of 25: (a) pure Mg, (b) Mg-0.5Gd, (c) Mg-1Gd, (d) Mg-3Gd, (e) Mg-6Gd, (f) Mg-9Gd, (g) Mg-12Gd, (h) Mg-15Gd, (i) Mg-18Gd.

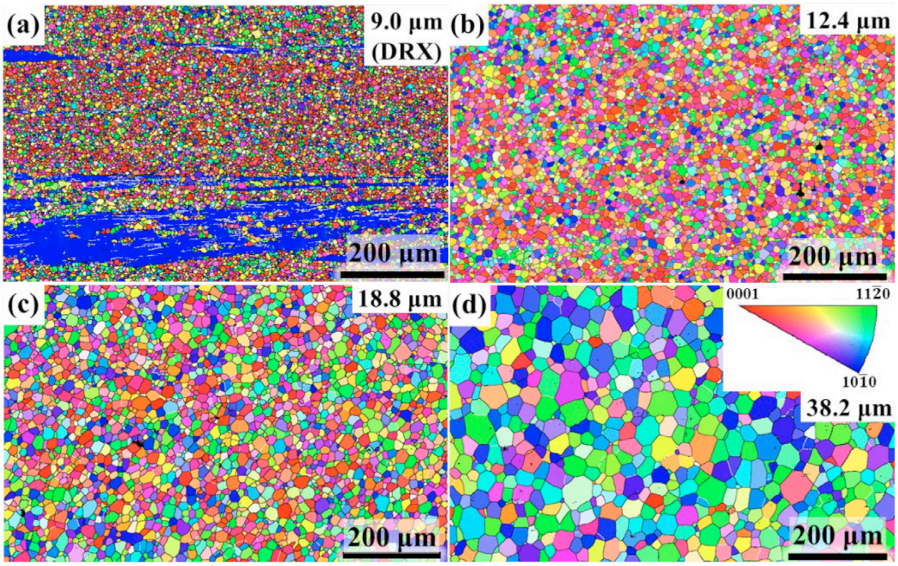

Fig. 3. EBSD IPF orientation maps (in the ED) of Mg-12Gd alloy extruded under different conditions: (a) at 350 °C with an extrusion ratio of 9, (b) at 350 °C with an extrusion ratio of 25, (c) at 400 °C with an extrusion ratio of 25, (d) at 500 °C with an extrusion ratio of 25. The corresponding average grain size (dynamically recrystallized grains) and the color coding for EBSD IPF maps are included as insets.

the Gd concentration is lower than its equilibrium solubility in Mg, the C-texture disappeared, and the basal texture was further enhanced to be the dominant texture component (Fig. 4(d)).

In summary, the above results prove that extrusion parameters, in particular the extrusion temperature, have a considerable effect on the texture of Mg-Gd alloy. Increasing extrusion temperature is able to realize the transformation between C-texture, RE texture and basal texture in the extruded Mg-Gd alloy.

To investigate the formation and transformation mechanism between basal texture, RE texture and C-texture, the interrupted extrusion experiments were conducted for pure Mg and Mg-18Gd alloy. Their microstructure evolutions with the strain inside extrusion die will be presented in the following sections.

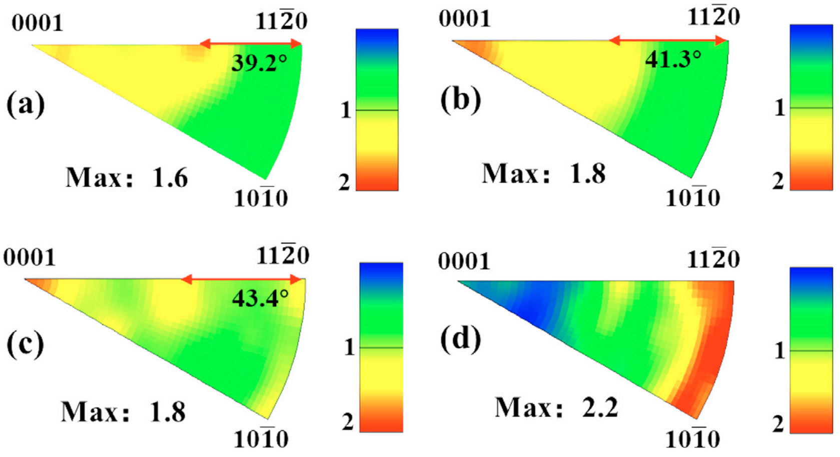

Fig. 4. Inverse pole figures (in the ED) of dynamically recrystallized microstructure of Mg-12Gd alloy extruded under different conditions: (a) at 350 °C with an extrusion ratio of 9, (b) at 350 °C with an extrusion ratio of 25, (c) at 400 °C with an extrusion ratio of 25, (d) at 500 °C with an extrusion ratio of 25.

3.3. Microstructure evolution of pure Mg and Mg-18Gd alloy with strain inside extrusion die

Fig. 5 compares the EBSD IPF orientation maps (in the ED) of pure Mg and Mg-18Gd binary alloy at different positions below the punch (see the inserts at the bottom). On one hand, the dynamic recrystallization area fraction of pure Mg increases with deceasing the distance to the die exit where plastic strain reaches its maximum. At 3.5 mm below the punch, the dynamic recrystallization has been initiated along the grain boundaries of deformed grains, as shown in Fig. 5(a). When the position moves to 10.5 and 17.5 mm, first formed is a bimodal microstructure with fine recrystallized grains and coarse unrecrystallized grains, and then the complete dynamic recrystallization microstructure in the pure Mg, as demonstrated by Figs. 5(b) and (c), respectively. On the other hand, the dynamic recrystallization in the Mg-18Gd alloy is severely impeded during extrusion. At 3.5 mm and 10.5 mm below the punch, there are only limited recrystallized grains, as shown in Figs. 5(d) and (e). Even at a closer position around the die exit, the dynamic recrystallization process still lags considerably, as shown in Fig. 5(f). Additionally, the recrystallized grain size in the Mg-18Gd alloy is much smaller due to the retardation of grain growth by the high-concentration Gd.

Besides, in the case of Mg-18Gd alloy, numerous lenticular configurations were captured in the microstructure at 3.5 mm and 10.5 mm below the punch. The EBSD results in Fig. 6 reveal that large amounts of tensile twins were activated and even to form crossing structures during the extrusion process of Mg-18Gd alloy [38], while the compressive twins and doubles twins were not activated, which can be evidenced by the absence of 56° and 38° $<11\bar{2}0>$ misorientation angle boundaries. It has been widely reported that the addition of RE elements can increase the activation stress of tensile twins by inhibiting the atomic shuffling process, thereby suppressing twining in the Mg alloys [15]. Conversely, in this study, profuse tensile twins are observed in the Mg-18Gd alloy during extrusion, while few of them are formed in pure Mg. The anomalous twinning behavior during extrusion of the pure Mg and Mg-18Gd alloy is assumed to be related with the difference in recrystallization process caused by Gd addition, which will be discussed later in more detail.

3.4. Microtexture evolution of pure Mg and Mg-18Gd alloy with strain inside extrusion die

Fig. 7 illustrates the EBSD inverse pole figures (in the ED) of pure Mg (a-c) and Mg-18Gd alloy (d-f) at different positions inside the extrusion die. In the pure Mg, an apparent $<10\bar{1}0>$//ED orientation along with a weak non-basal texture component has been established at the early state of extrusion (at 3.5 mm, see Fig. 7(a)). With the successive occurrence of dynamic recrystallization, the extrusion texture at 10.5 mm was weakened slightly (Fig. 7(b)). Finally, a typical basal texture with an intensity of 3.8 MRD developed in the front of the die exit (at 17.5 mm).

During the extrusion of Mg-18Gd alloy, a typical basal texture ($<10\bar{1}0>$-$<11\bar{2}0>$//ED) with a maximum intensity of 6.1 MRD was formed at the early stage (at 3.5 mm below the punch, see Fig. 7(d)). Further straining strengthened the basal texture, making the orientation more concentrated at 10.5 mm and 17.5 mm (Figs. 7(e)-(f)). It is clear that a stronger basal deformation texture was established throughout the extrusion process of Mg-18Gd alloy in comparison with pure Mg owing to limited dynamic recrystallization.

3.5. Comparison of drx mechanism between pure Mg and Mg-18Gd alloy and its effect on texture development

In order to reveal the formation mechanism of different texture components, the effect of Gd on dynamic recrystallization mechanism and on texture development of Mg alloy was investigated by EBSD measurements. Fig. 8 shows the enlarged view of a typical recrystallization area that is enclosed within the red rectangle in Fig. 5(b). It is clear that the dynamic recrystallization mainly starts at the grain boundaries in pure Mg. Moreover, the deformed grain boundaries

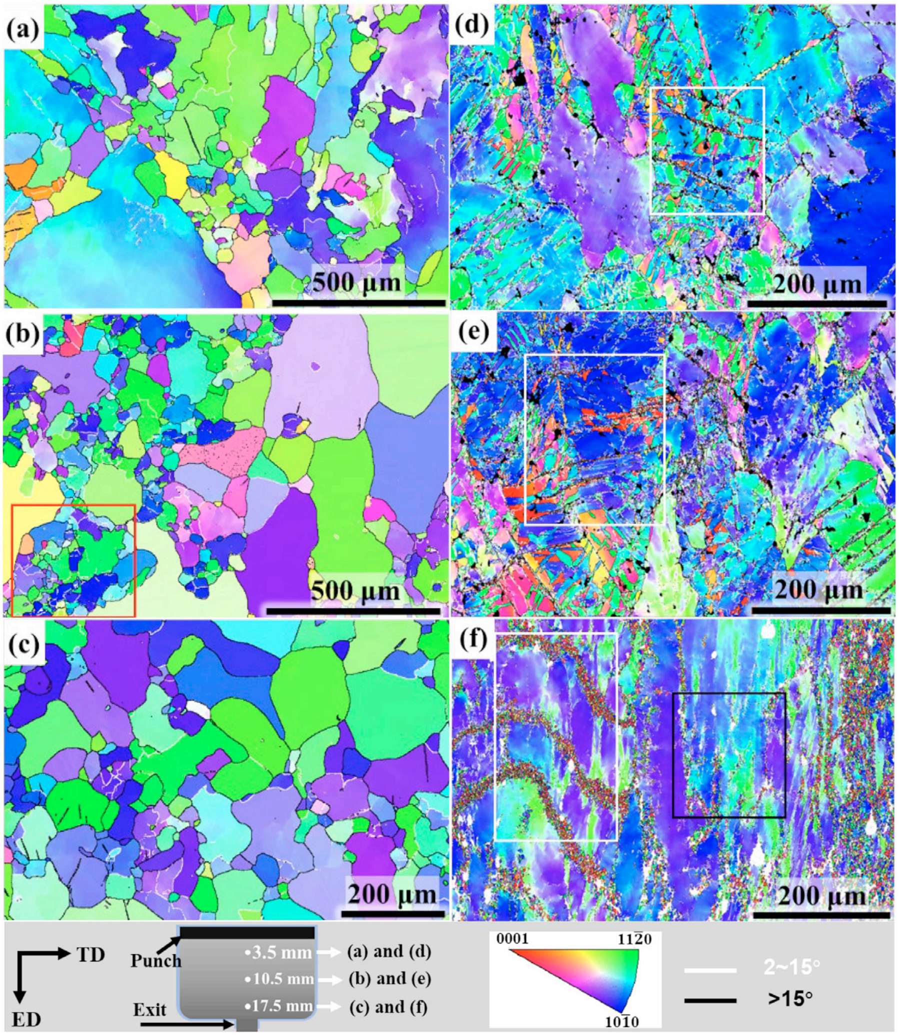

Fig. 5. EBSD IPF orientation maps in the extrusion direction (ED) of pure Mg (a-c) and Mg-18Gd alloy (d-f) at different positions inside extrusion die during extrusion at 350 °C with a ratio of 25: (a) and (d) at 3.5 mm below the punch, (b) and (e) at 10.5 mm below the punch, (c) and (f) at 17.5 mm below the punch. The schematic graph of extrusion and the color coding for the EBSD maps are included as an inset. Areas enclosed by red, white and dark rectangles will be further analyzed below.

exhibit to be highly mobile during extrusion at 350 °C with an extrusion ratio of 25. Several segments of grain boundaries, as highlighted by the red arrows in Fig. 8(a), are observed to be bowed out, which is a salient feature of the discontinuous dynamic recrystallization. As demonstrated by the line profile of misorientation angle along the white arrow spreading from one side of deformed grain to the other, the apparent misorientation variation only appears when the arrow intersects with a low angle boundary (see Fig. 8(d)), indicating the intragranular relative rotation induced by internal strain. Also, the small point-to-point misorientation angle demonstrates the low dislocation density within the deformed grains, which is consistent with the discontinuous dynamic recrystallization process (DDRX). The other dynamic recrystallization mechanisms, such as continuous (CDRX) and twinning-induced dynamic recrystallization seems to be suppressed during extrusion of pure Mg at 350 °C with an extrusion ratio of 25. The orientation of recrystallized microstructure along $<10\bar{1}0>$-$<11\bar{2}0>$ boundary of the unit triangle (Figs. 8(b)-(c)), as well as the misorientation peak at 30° (Fig. 8(e)) indicate that the preferential nucleation and growth of DDRXed grains with specific orientation (30° <0001> relative to the host deformed parent grains), which is in agreement with the previous studies [39].

In contrast with the extrusion deformation of pure Mg, the microstructure evolution of Mg-18Gd alloy, during extrusion at 350 °C with an extrusion ratio of 25, is barely affected by the discontinuous dynamic recrystallization. The absence of recrystallized grains at the deformed grain boundaries in Mg-18Gd alloy (see Figs. 5(d)-(e)) provides clear evidence that the severe suppression of discontinuous dynamic recrystallization by the high-concentration Gd element. The IPF map (in the ED) in Fig. 9(a) is the enlarged view of the boxed area by dark rectangle in Fig. 5(f). It illustrates that only a small number of recrystallized grains are formed along the boundaries of deformed grains in the Mg-18Gd alloy near the die exit during extrusion. Owing to the limited recrystallization, a high

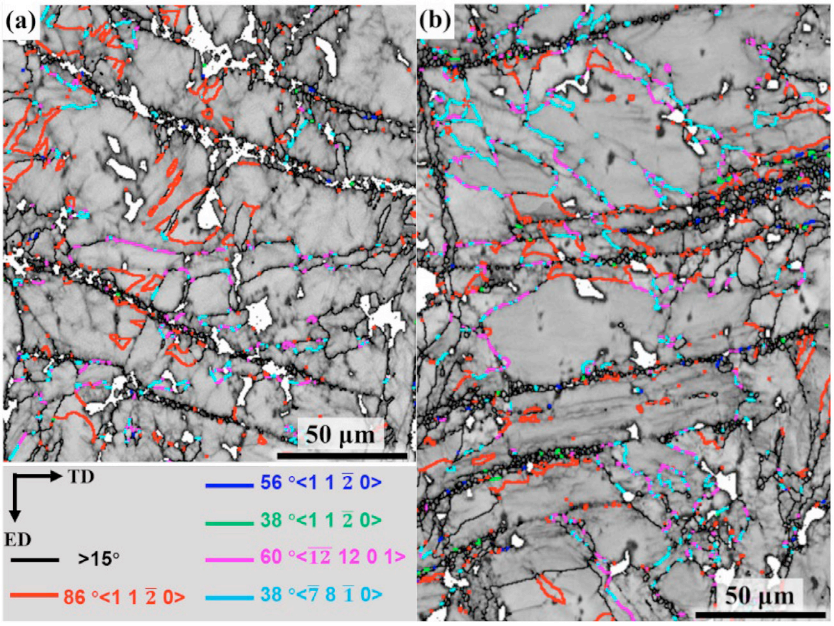

Fig. 6. The twin distribution from the boxed areas in Figs. 5(d) and (e): (a) at 3.5 mm, (b) at 10.5 mm. The boundaries of different twin variants are highlighted by lines with different colors, as shown in the insert.

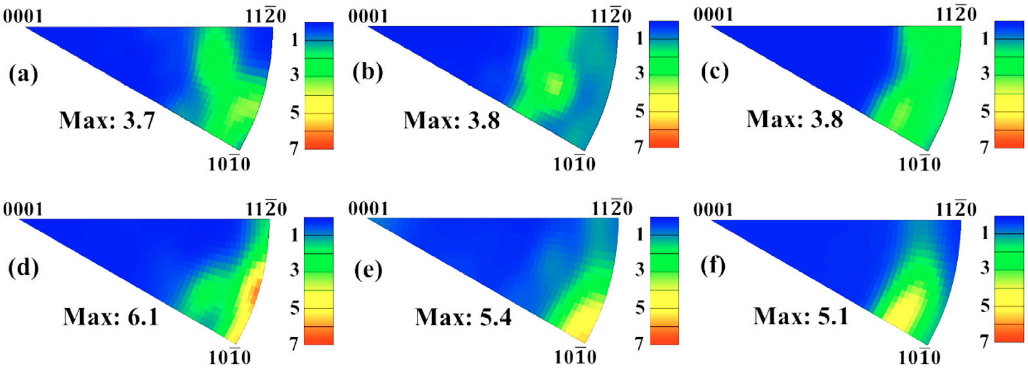

Fig. 7. EBSD inverse pole figures in the extrusion direction (ED) of pure Mg (a-c) and Mg-18Gd alloy (d-f) at different positions inside extrusion die during extrusion at 350 °C with an extrusion ratio of 25: (a) and (d) at 3.5 mm, (b) and (e) at 10.5 mm, (c) and (f) at 17.5 mm.

density of dislocation was accumulated within the deformed grains, leading to a large misorientation (Fig. 9(d)). The inverse pole figures of unrecrystallized grains and recrystallized grains were plotted separately (Figs. 9(b) and (c)) to reveal the effect of discontinuous dynamic recrystallization on the texture evolution of Mg-18Gd alloy. As what occurred in the pure Mg, the discontinuous dynamic recrystallization did not perturb the basal fiber texture of Mg-18Gd alloy, only leading to a relative rotation from (10$\bar{1}$0) pole to (11$\bar{2}$0) pole along the boundary of stereographic triangle, generating a peak at 30° in misorientation distribution histogram (Fig. 9(e)). Hence, the RE-texture and abnormal C-texture in the extruded Mg-18Gd alloy shall not originate from the discontinuous dynamic recrystallization.

In comparison with discontinuous dynamic recrystallization along the grain boundaries, continuous dynamic recrystallization within grains seems to have more important effect on the microstructure evolution of Mg-18Gd alloy during extrusion. In order to gather more information, the enlarged view of typical continuous dynamic recrystallization areas, which are enclosed within white rectangles in Figs. 5(d)-(f), are illustrated in Fig. 10 (the corresponding unrecrystallized microstructures are provided in supplement, see Fig. S1). It shows that the nucleation of dynamical recrystallization grains in the deformed grains is highly heterogeneous, confined within some very narrow shear bands, approximately 10 μm to 30 μm in width (see Figs. 10(a)-(c)). With increasing strain (moving from 3.5 mm to 17.5 mm below the punch), the dynamic recrystallization is enhanced by activating more shear bands and by increasing the width of shear bands. By contrast, the nucleation of dynamic recrystallization outside the shear bands is not apparent even near the die exit (at 17.5 mm). Figs. 10(a1)–(c1) depict the corresponding inverse pole figures of recrystallized grains within shear bands. It is worth noting that recrystallization within shear bands in the sample at 3.5 mm, where the strain is smaller,

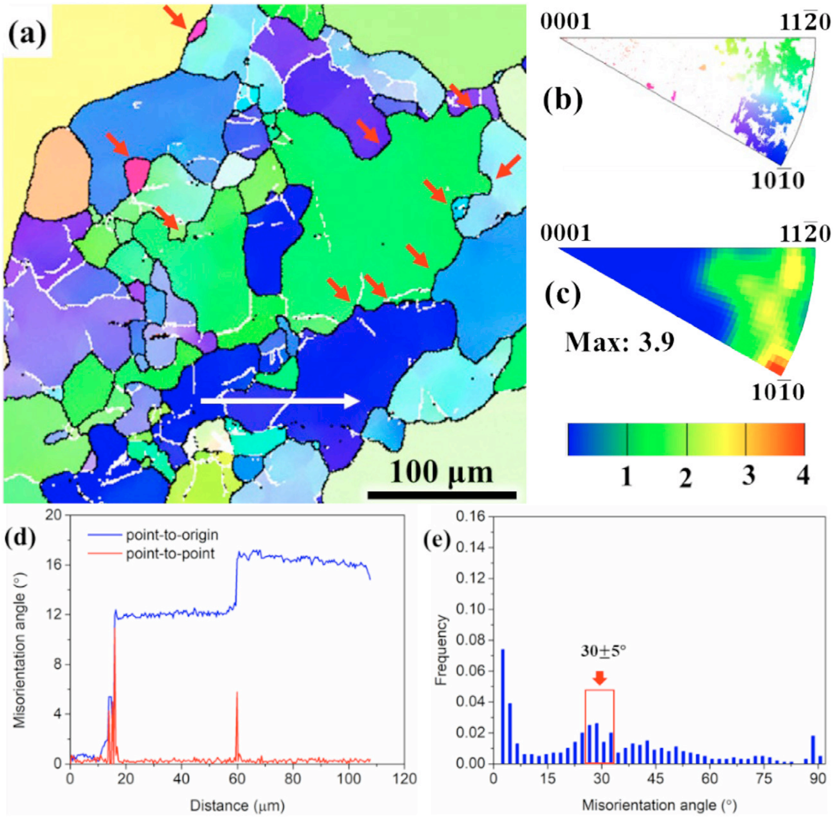

Fig. 8. The enlarged view of a typical recrystallization area enclosed within the red rectangle in Fig. 5(b): (a) EBSD IPF map, as well as the corresponding inverse pole figures (b) (scatter plot) and (c) (after calculation), (d) line profiles of misorientation angle along the white arrow in Fig. 8(a), (e) misorientation angle distribution.

yields a faint basal fiber texture along the $<10\bar{1}0>$-$<11\bar{2}0>$ boundary of unit triangle and a weaker RE texture orienting 51.5° far from the $(11\bar{2}0)$ pole. Further straining weakens the basal fiber texture component, reoriented the RE texture from 51.5° to 59° far from the $(11\bar{2}0)$ pole, and lead to the formation of C-texture component in dynamically recrystallized microstructure within shear bands (at 10.5 mm, see Fig. 10(b1)). Near the extrusion die exit (at 17.5 mm below the punch) the orientation of dynamically recrystallized grains within shear bands becomes more concentrated, only the C-texture component with a preferred alignment of ED with (0001) pole is apparent in the inverse pole figure (Fig. 10(c1)). Therefore, it can be envisaged that the orientation of dynamically recrystallized grains within shear bands experience a substantial rotation as the strain increases during extrusion.

In summary, the results above reveal that discontinuous dynamic recrystallization, a prominent recrystallization mechanism in the extruded pure Mg, is severely suppressed in the extruded Mg-18Gd alloy, thus impeding the development of basal extrusion texture. Moreover, the recrystallized grains (CDRX), with a similar orientation with the host deformed parent grain (along the $<10\bar{1}0>$-$<11\bar{2}0>$ boundary of unit triangle), are nucleated within the shear bands, and then they are successively reoriented to (0001) pole during nucleuses growth, undergoing an intermediate configuration with the RE-texture orientation. We will unravel the formation mechanism of shear bands in the following sections by combining the IGMA analysis and TEM characterization.

4. Discussion

4.1. Dynamic recrystallization mechanism and the effect of RE

Three primary dynamic recrystallization mechanisms have been proposed in Mg alloys based on the operating deformation mechanism, including discontinuous dynamic recrystallization (DDRX), continuous dynamical recrystallization (CDRX), and twinning-induced dynamical recrystallization (TDRX) [40,41]. Among them, DDRX occurs via grain boundary migration, which is accompanied with the nucleation and growth of strain-free new gains from grain boundaries. By contrast, CDRX results from dislocation accumulation, a gradual process with low-angle boundaries successively evolving into high-angle boundaries. TDRX has a similar nucleation mechanism with CDRX except that nucleation preferentially occurs in twin regions. In the deformation process of Mg alloys, the prevalence of one or the other depends, however, not only on the deformation conditions but also on the alloy's composition.

Earlier studies have highlighted the temperature-dependent nature of the dynamic recrystallization mechanism. For exam-

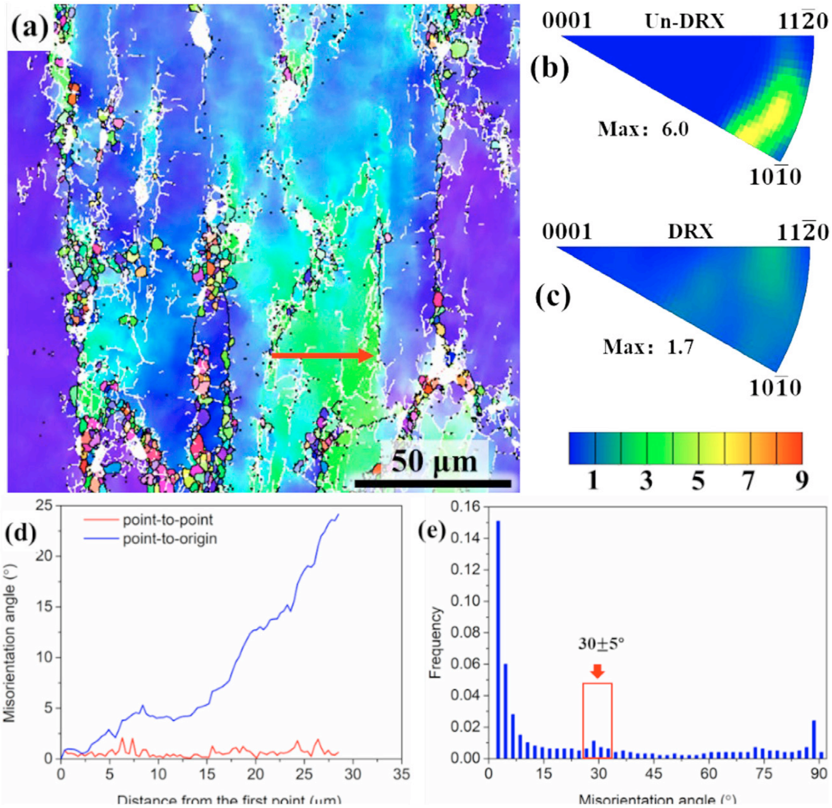

Fig. 9. The enlarged view of a typical area with limited dynamic recrystallization along grain boundaries enclosed within the dark rectangle in Fig. 5(f), (a) EBSD IPF map, as well as the corresponding inverse pole figures of unrecrystallized microstructure (b) and recrystallized microstructure (c), respectively, (d) line profiles of misorientation angle along the red arrow in Fig. 9(a), (e) misorientation angle distribution.

ple, in ZK60 alloy, the activation of TDRX prevails during deformation at low temperatures (below 200 °C). At intermediate temperatures (200 °C – 250 °C), CDRX is the dominant mechanism, while at high temperatures (> 300 °C), DDRX is notably enhanced [40]. Owing to the higher mobility of grain boundaries in pure Mg than compared to the ZK60 alloy, the extrusion process of pure Mg at 350 °C in this study appears to be dominated by the DDRX (Fig. 8). Alloying with rare earth elements was reported to retard dynamic recrystallization [42–46]. On one hand, alloying with RE elements not only increase the stress required for dislocations gliding, but also inhibit the cross-slip and climb of dislocations, i.e., nucleation process of CDRX [47–49]. On the other hand, segregation of rare earth elements to grain boundaries can effectively reduce the boundary mobility, thus restricting the DDRX [50,51]. Moreover, dynamic precipitation cannot be avoided completely in the Mg-18Gd alloy during extrusion (some areas with poor indexing in Fig. 11), and thus affect the microstructure evolution. The earlier studies [52] have evidenced that the presence of particles will enhance the dynamic recrystallization process, i.e. particle-stimulated nucleation recrystallization. However, in comparison with the retardation of the high-concentration solid solution atoms on the dynamic recrystallization, the effect of particle-stimulated nucleation on dynamic recrystallization is much smaller in the solid solution treated alloy. Therefore, after the addition of high-concentration Gd element, the nucleation of dynamic recrystallization, in particular by grain boundaries migration (DDRX), is dramatically inhibited in the Mg-18Gd alloy (see Fig. 5). This eventually gives rise to a strong basal fiber texture (see Fig.7) that is characteristic of high-density dislocations distributed inhomogeneously in the deformed grains, as evidenced by Fig. 11. Therefore, either the non-basal slip, which is infrequent in the pure Mg, or the deformation twin that is assumed to be inhibited in high alloyed Mg alloys has a high propensity to be activated during extrusion.

4.2. Shear bands and the effect of deformation mechanism

Shear bands are narrow zones with intense shear strains, the local areas of heterogeneous plastic deformation that provide an extensive internal misorientations [53]. They are nucleated by the discrete slips and twins at the microscale and can pass through several grains or even extend through the specimen, leading to flow instability at macroscale [54]. Plastic deformation of Mg alloys is highly anisotropic due to comparatively very low CRSS of basal slip, which can only accommodate the strain along the **<a>** axis, with respect to that of non-basal slip, rendering the deformation along the **<c>** axis much harder. As a consequence, the development of shear bands is prevalent during the severe plastic deformation of pure Mg and Mg alloys both in the single-crystalline [29,49] and polycrystalline specimens [22,26,62,63,54–61]. The ori-

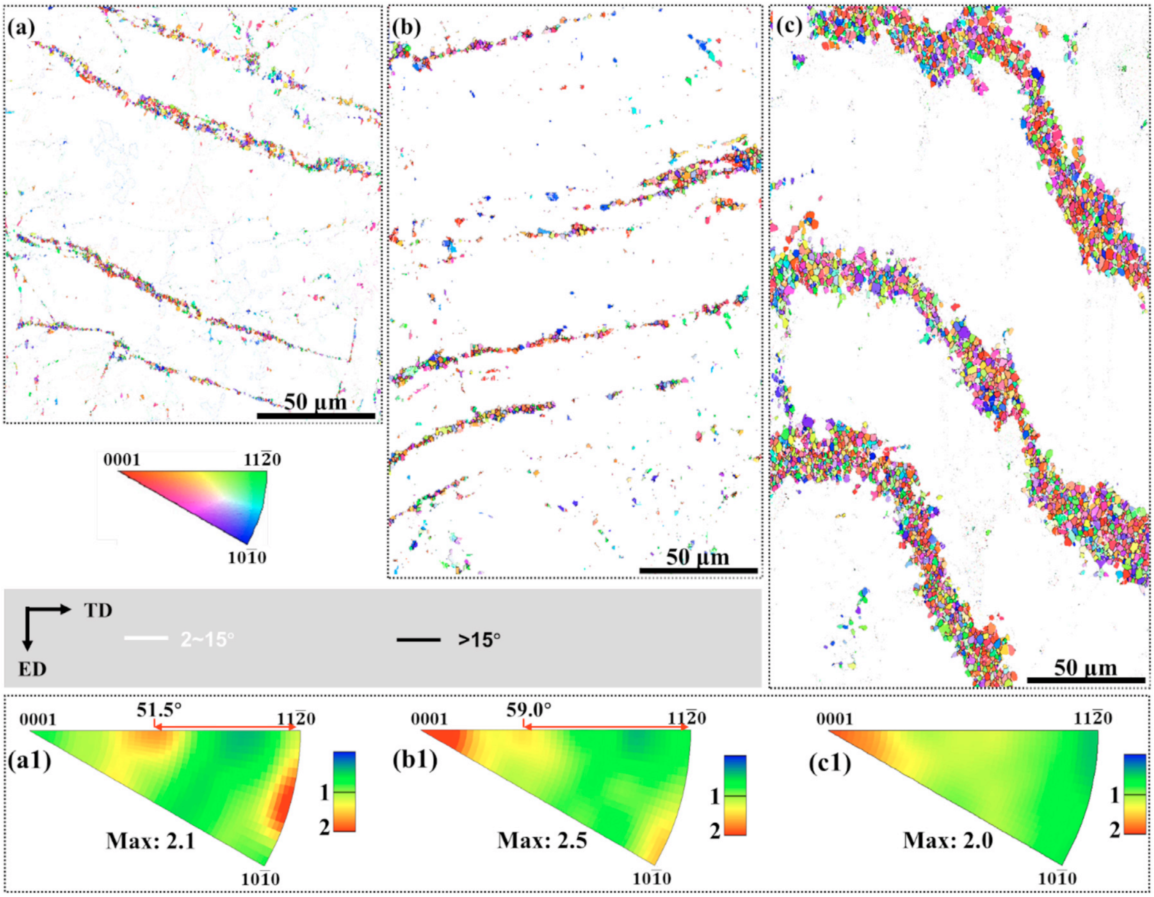

Fig. 10. The recrystallized microstructure in areas enclosed within white rectangles in Figs. 5(d)-(f). (a) and (a1) the recrystallized microstructure in the area enclosed within white rectangle in Fig. 5(d) and the corresponding inverse pole figure, (b) and (b1) the recrystallized microstructure in the area enclosed within white rectangle in Fig. 5(e) and the corresponding inverse pole figure, (c) and (c1) the recrystallized microstructure in the area enclosed within white rectangle in Fig. 5(f) and the corresponding inverse pole figure.

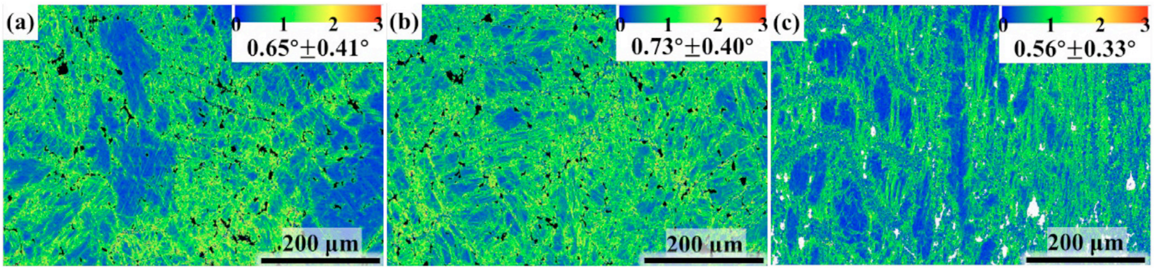

Fig. 11. KAM maps of the Mg-18Gd alloy samples at different positions inside extrusion die: (a) at 3.5 mm, (b) at 10.5 mm, (c) at 17.5 mm. The average KAM value is included as an insert in the corresponding map.

gin of shear bands in Mg alloys remains, however, unclear because of the complex dislocation-twin interaction.

Twinning-induced shear band, mainly by the {10$\bar{1}$1} compression twin or by {10$\bar{1}$2}-{10$\bar{1}$1} double twin, was evidenced to be an important mechanism in the Mg-RE alloy. According to our EBSD results (see Fig. 6), however, only tension twins are active during the extrusion of Mg-18Gd alloy at 350 °C, while the activation of compression or double twins is restricted. This indicates that the mechanism of double twinning in promoting nucleation of shear bands might not apply to our study. Recently, it has been demonstrated that slip either on the basal or on the pyramidal plane can also trigger the shear bands at micro scale [29,49,61]. In order to reveal the origin of shear bands in the Mg-18Gd alloy, several typical areas with shear bands were extracted for further analyses. The analyzed results are presented in Fig. 12. Note that multiple dark grey lines, aligned with the shear bands where dynamic recrystallization preferentially occurs, are present in the microstructure of extruded Mg-18Gd alloy, as highlighted by the red arrows in Figs. 12(a) and (d). The darker contrast of these grey lines is indicative of a higher geometrically necessary dislocation density on the corresponding crystallo-

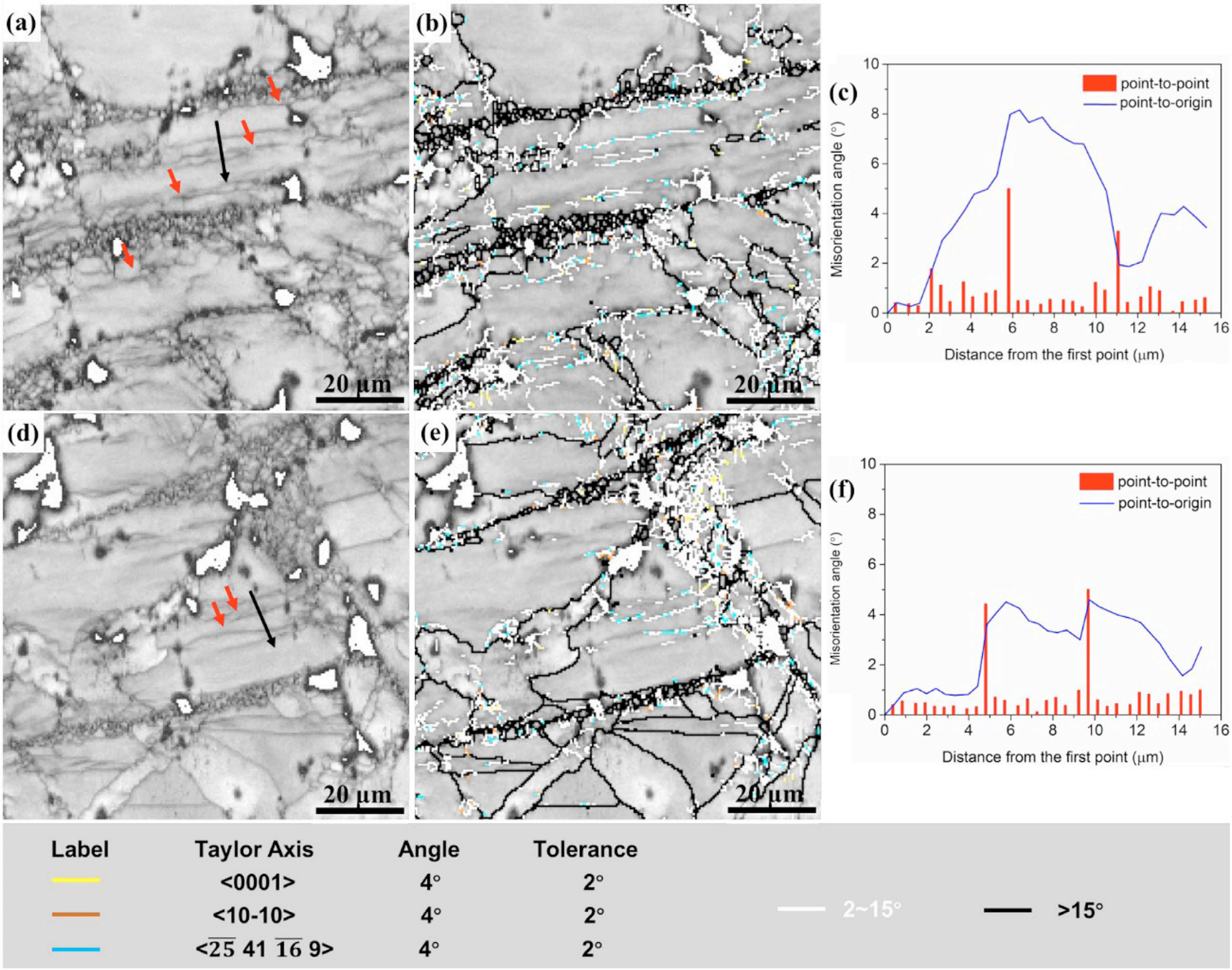

Fig. 12. Band contrast maps of areas with shear bands in the extruded Mg-18Gd alloy at 10.5 mm below the punch. The low-angle grain boundaries (2–15°), high-angle grain boundaries (>15°), as well as special low-angle boundaries with a misorientation 2–6° corresponding to different intragranular misorientation axes (IGMA) were plotted using lines with different colors (see inserts at the bottom of figures).

graphic planes that are favorable for the occurrence of dynamic recrystallization. For this reason, these dark grey lines can be considered as precursors of shear bands. From the line profiles of misorientation angle along the dark arrows in Figs. 12(a) and (d), it can be seen that there is a minor jump with only 4–6° in misorientation angle when the arrows intersect with these dark grey lines (see Figs. 12(c) and (f)). The measured misorientation is much smaller than that triggered by compression twin (~56°) or double twin (~38°). Such minor misorientation change is usually related to the pile-up of geometrically necessary dislocations.

To reveal the corresponding slip modes that lead to the slip localization, IGMA analysis was also conducted. In principle, the low-angle boundaries with IGMA lying around (0001) are triggered by the pile-up of prismatic <a> dislocations, while the low-angle boundaries with the IGMA along $\langle 10\bar{1}0\rangle$-$\langle 11\bar{2}0\rangle$ boundary of unit triangle correspond to the basal <a> and $\{10\bar{2}2\}$ $\langle 11\bar{2}3\rangle$ pyramidal II dislocations [64]. $\{10\bar{1}1\}$ $\langle 11\bar{2}3\rangle$ pyramidal I slip in the hcp structure with an ideal c/a ratio has the IGMA of $\langle \overline{25}\ 41\ \overline{16}\ 9\rangle$ [8]. As shown in Figs. 12(b) and (e), a part of the low-angle boundary segments along the dark grey lines or near shear bands possess the $\langle \overline{25}\ 41\ \overline{16}\ 9\rangle$ Taylor axis. A TEM lamella traversing dark grey lines was also milled, as highlighted in blue in the band contrast EBSD map of Fig. 13(a), to further examine the corresponding dislocation structures of the low angle boundaries. The corresponding TEM results are presented in Figs. 13(b)-(f). Fig. 13(b) represents a typical low angle grain boundary, consisting of tangled dislocations. The dislocation structures of low-angle boundary appear to be composed of a large array of rectilinear dislocations, that are aligned with the prismatic plane under $\boldsymbol{g}$=[0002]. Some of the rectilinear dislocations, as indicated by the blue arrows in Fig. 13(c), are still visible under $\boldsymbol{g}=[10\bar{1}0]$ and $\boldsymbol{g}=[10\bar{1}1]$, but they are invisible under $\boldsymbol{g}=[10\bar{1}\bar{1}]$. According to the $g \cdot b = 0$ invisibility criteria, these dislocations indicated by the blue arrows

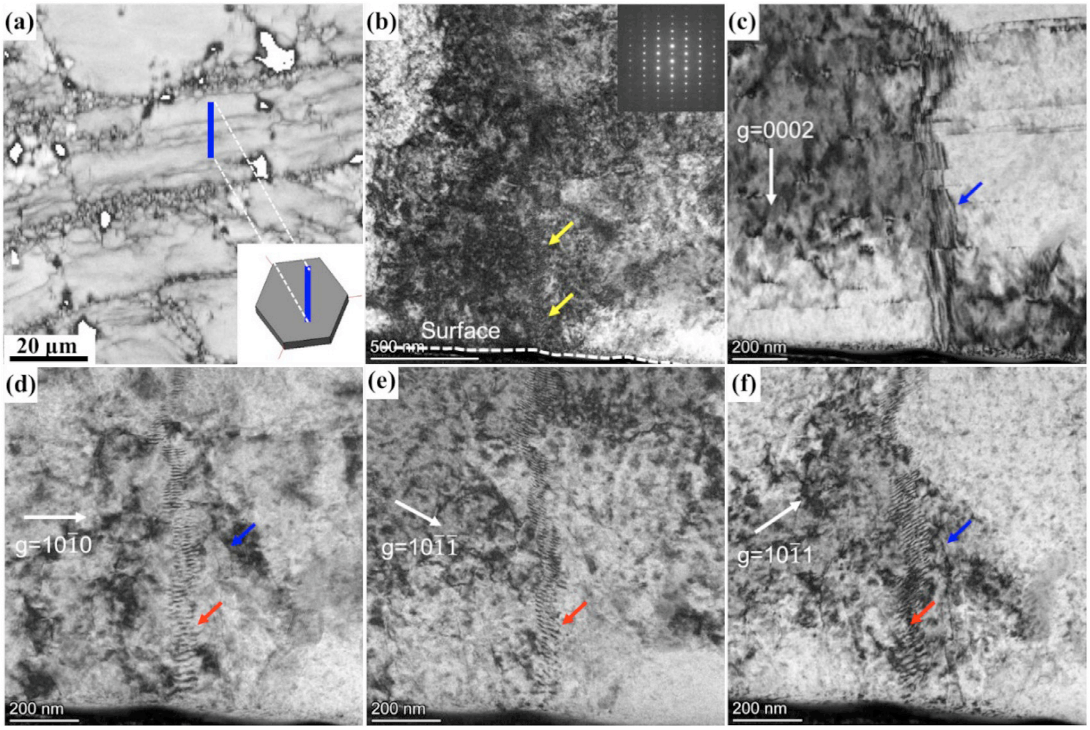

Fig. 13. (a) Band contrast map showing, in blue, the location of where the lamella was milled. (b) The bright field TEM image showing the low angle grain boundary in Fig. 13(a). (c)-(f) Bright-field TEM images of dislocation structures taking under different diffraction conditions.

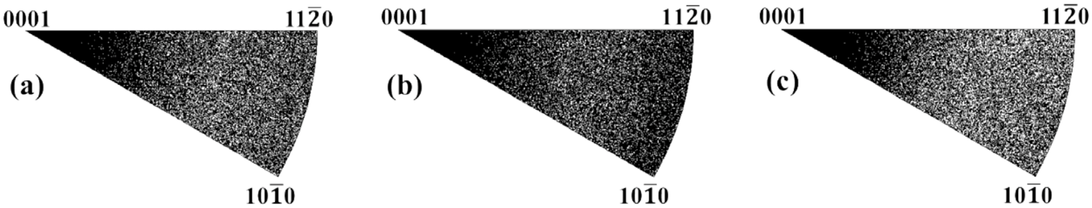

Fig. 14. IGMA distribution of the low-angle grain boundaries (2–6°) in the samples of Mg-18Gd alloy at 3.5 mm (a), 10.5 mm (b) and 17.5 mm (c) below the punch.

in Figs. 13(c), (d) and (f) are perfect <**c** + **a**> dislocations with the Burgers vectors $\boldsymbol{b} = 1/3[11\bar{2}3]$ or $\boldsymbol{b} = 1/3[\bar{2}11\bar{3}]$. Besides, a regular dislocation array with the dislocations lying on the basal plane and with the stacking direction perpendicular to the basal plane is observed under $\boldsymbol{g}=[10\bar{1}0]$, $\boldsymbol{g}=[10\bar{1}\bar{1}]$ and $\boldsymbol{g}=[10\bar{1}1]$, but which is invisible under $\boldsymbol{g}=[0002]$, thus the regular dislocation array is composed of <**a**> dislocations. Comparative analysis of the Taylor axis and TEM results, we can prove the critical role of $\{10\bar{1}1\}$ $<11\bar{2}3>$ pyramidal I slip system in promoting the formation of shear bands.

Owing to its higher energy and CRSS with respect to the $\{10\bar{2}2\}$ $<11\bar{2}3>$ pyramidal II dislocations, the $\{10\bar{1}1\}$ $<11\bar{2}3>$ pyramidal I slip system is usually overlooked in the previous studies for considering its contribution to promoting the nucleation of DRX and modifying the deformation texture of Mg alloys. Solutes, especially RE elements, however, have been evidenced to reduce the energy of pyramidal I dislocation, to enable its mobility and even to switch it to be the primary <c + a> slip system with the solute concentration exceeding a limit (3.55 wt.% for Gd) [17]. The profuse activation of pyramidal I dislocations was also reported in the deformation of Mg-(0.6–1.1) at.% Y single crystals along the c-axis or in the textured polycrystals [65].

Apart from preceding local shear bands, we also performed the statistics analysis of the IGMA in the large areas presented in Figs. 5(d)-(f). The concentration of IGMA around (0001) pole throughout the entire deformation stage is shown in Fig. 14. It illustrates that the extrusion of Mg-18Gd alloy is dominated by the prismatic <a> dislocations. In addition, the high-density and dispersive distribution of IGMA in the entire unit triangle reveal the extensive activation of other slip systems, as well as the strong dislocation interactions. However, if we take a closer inspection of the deformed grains (see Fig. S2 in the supplement), where the prismatic slip is prevalent but pyramidal slip is scarce, shear bands and the

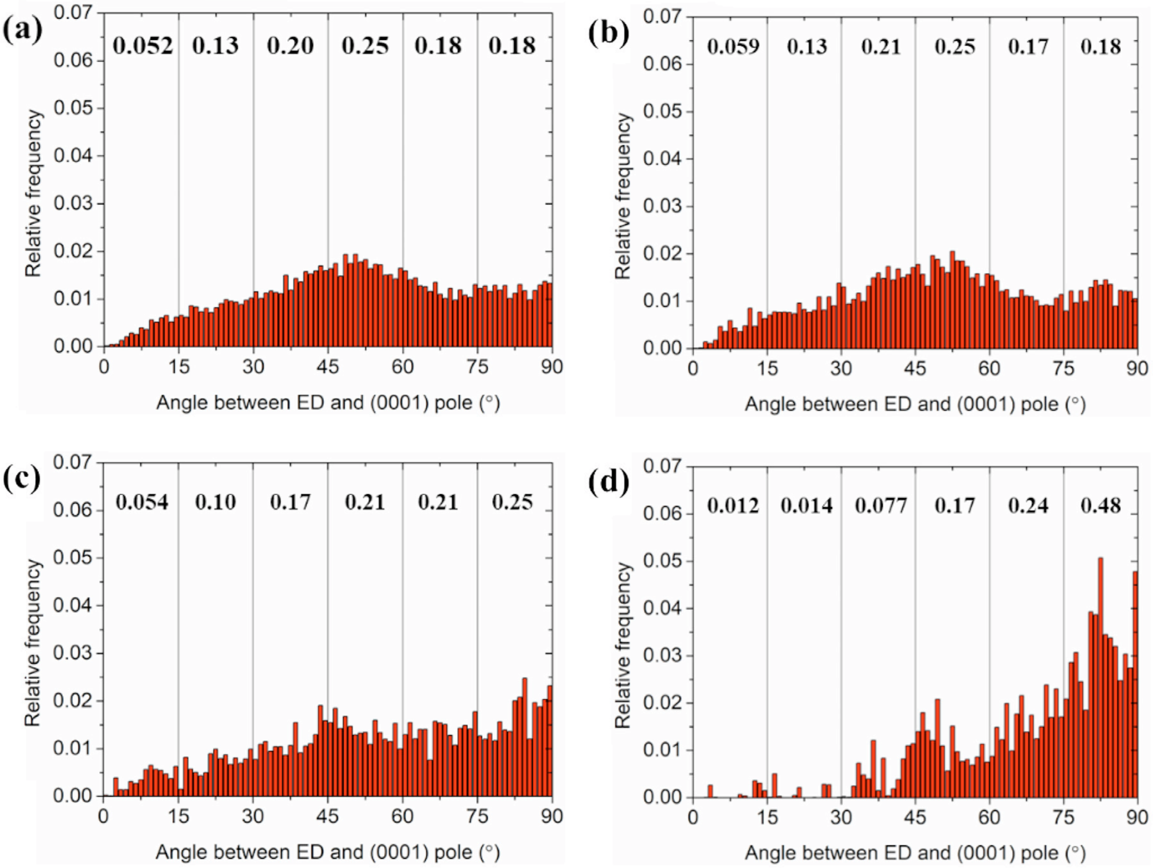

Fig. 15. A quantitative analysis of the relative orientation between c-axis of grains and the ED of Mg-12Gd alloy extruded under different conditions: (a) at 350 °C with an extrusion ratio of 9, (b) at 350 °C with an extrusion ratio of 25, (c) at 400 °C with an extrusion ratio of 25, (d) at 500 °C with an extrusion ratio of 25.

resultant dynamical recrystallization do not appear, indicating the sole operation of prismatic <a> slip cannot induce shear bands and the resultant heterogeneous nucleation of DRX.

In summary, although the prismatic <a> slip is the predominant deformation mechanism during the extrusion of Mg-18Gd alloy, the pyramidal I dislocations are also profusely yet heterogeneously activated. The heterogeneous activation of profuse pyramidal I dislocations facilitate the formation of shear bands, providing the sites for dynamic recrystallization nucleation in the high-concentration Mg-Gd alloy during extrusion.

4.3. Nucleation of dynamic recrystallization and orientation evolution in Mg-Re alloys

As aforementioned, CDRX within shear bands dominates the microstructure evolution of Mg-18Gd alloy, and it has a profound effect on the recrystallization texture. For this reason, the following discussions will be concentrated on the nucleation of dynamic recrystallization within shear bands. As shown in Fig. 10(a1), the nucleuses of dynamic recrystallization within shear bands at the initial stage of deformation (at 3.5 mm below the punch, where the strain is relatively smaller) have a similar orientation with the host deformed parent grains (see Fig. S1(a1)). This is in agreement with previous studies that recrystallized grains arising from both continuous and discontinuous subgrains growth usually have the same orientation with the host deformed parent grains [22,26,66]. From the observation in Fig. 11(a1) that the RE texture component tilts 51.5° away from the $(11\bar{2}0)$ pole, it is reasonably deduced that a small number of recrystallized grains has reoriented either at nucleation stage or during the subsequent subgrain growth process. With increasing strain (moving the observation position to 10.5 mm and 17.5 mm below the punch), there is an increasing proportion of recrystallized grains within shear bands that are reoriented by tilting their c-axis farther from the $<10\bar{1}0>$-$<11\bar{2}0>$ boundary of unit triangle, yielding the C-texture orientation with c-axis aligned with the extrusion direction (Figs. 10(b1) and (c1)). The RE orientation seems to be a transition stage during the reorientation process of recrystallized grains from $<10\bar{1}0>$-$<11\bar{2}0>$ boundary of unit triangle to (0001) pole in the Mg-18Gd alloy. As a consequence, the recrystallized grains either with the RE-texture orientation or with the C-texture orientation are initially nucleated with $<10\bar{1}0>$-$<11\bar{2}0>$//ED orientation, but they are gradually tilted their c-axis to ED during nucleuses growth by successively absorbing dislocations, which can be considered as an extensive recovery process [49].

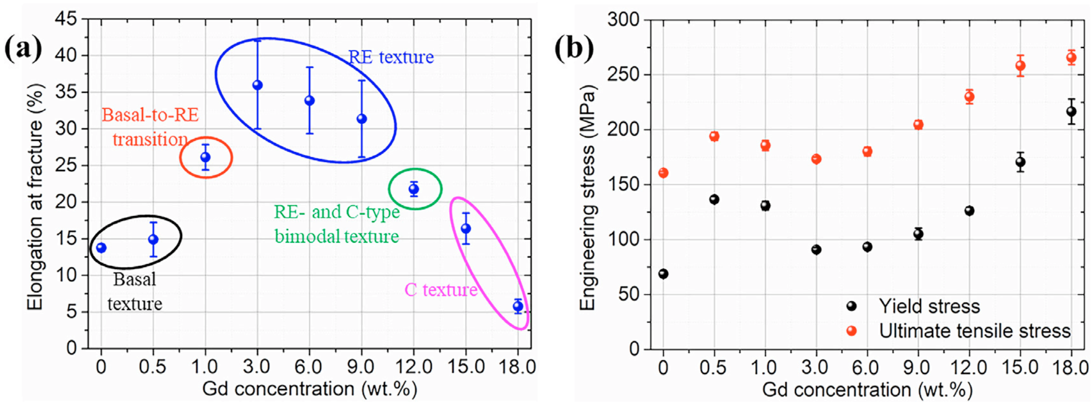

Fig. 16. Summary of mechanical properties of pure Mg and Mg-Gd alloys extruded at 350 °C with an extrusion ratio of 25.

As reported earlier [27,67], the prevalence of basal and prismatic slip contributes to the formation of recrystallization texture with $<11\bar{2}0>$//ED during extrusion of Mg alloys, which will be further enhanced during the grain growth owing to a relative lower energy and higher mobility of the 30° $<0001>$ grain boundaries [39]. Only the pyramidal slip is able to reorient the recrystallized grains with their c-axis tilting to ED [28,31,32]. As analyzed above, pyramidal I slip is profusely activated along the shear bands, so it is in favor of the nucleus reorientation process.

In conclusion, the texture evolution of Mg-Gd alloy can be recapitulated to be a strong basal deformation fiber texture that is developed due to the strong effects of RE atoms on reducing the mobility of dislocations and grain boundaries, thus retarding the nucleation of dynamic recrystallization. The preferential orientation of deformed grains with limited DRX can facilitate the activation of non-basal slip due to strain hardening of basal slip and high Schmid factor of non-basal slip. Moreover, the addition of RE elements can reduce the CRSS ratio between basal <a> slip and non-basal slip, thus enhancing the activation of non-basal slip, in particular of the $<c + a>$ pyramidal slip. Then, the heterogeneous operation of pyramidal slip during low-temperature extrusion causes the formation of shear bands and the resultant nucleation of dynamic recrystallization within shear bands with an initial orientation that is similar with the host deformed parent grains. Next, nucleuses gradually grow by successively absorbing pyramidal dislocations within or near shear bands, which can be seen as a recovery process, along with tilting their c-axis to ED. Finally, the tilting angle between c-axis of DRXed grains and ED, as well as the location of maximum pole intensity (to form RE-texture or C-texture) depends on the store energy within shear bands provided by the pyramidal slip.

It is expected that we can manipulate the relative orientation of grains quantitively based on the in-depth understanding of the formation mechanism of the extrusion texture in Mg alloys by controlling the deformation parameters (tailoring store energy within shear bands). On one hand, increasing the deformation temperature can not only improve the mobility of grain boundaries, but also reduce the propensity of strain localization (decreasing the store energy within shear bands). It thus can promote the nucleation by grain boundary migration and weaken the nucleation process within shear bands. As a result, the basal fiber texture component will be enhanced, while the RE-texture component and C-texture component will be weakened. Figs. 15(b)-(d) illustrates the quantitative analysis results of the grain orientation of Mg-12Gd alloy extruded at different temperatures with an extrusion ratio of 25. Extrusion at 350 °C (Fig. 4(b) and Fig. 15(b)) exhibits a relatively stronger C-texture component and a weaker RE-texture component, with 19% grains tilting their c-axis to the ED (the angle between c-axis and (0001) pole is smaller 30°, i.e. C-texture component) and 18% grains tilting their c-axis far from the ED (the angle between c-axis and (0001) pole is greater 75°). Increasing the extrusion temperature to 400 °C, the area fraction of grains tilting their c-axis far from the ED increases up to 25%. Further increasing the extrusion temperature to 500 °C, the fraction of grains tilting their c-axis far from the ED increases sharply up to 48%. Moreover, since strain localization is eliminated, only 2.6% grains tilt their c-axis to the ED. On the other hand, decreasing the extrusion strain can also alleviate the propensity of strain localization, and it in turn weakens the C-texture component. As shown in Figs. 15(a) and (b), the area fraction of grains tilting their c-axis to the ED decreases slightly from 19% to 18% with the extrusion ratio reducing from 25 to 9.

4.4. The effect of texture evolution on the mechanical properties

Fig. S3 illustrates the tensile engineering stress-engineering strain curves of pure Mg and Mg-Gd binary alloys extruded at 350 °C with an extrusion ratio of 25, and the corresponding elongation at fracture and tensile stress were summarized in Fig. 16. From Fig. 16(a), it can be clearly seen that the Mg-Gd binary alloys with the RE texture have an excellent fracture elongation, exceeding 30%. The Mg-Gd binary alloys with the intermediate texture configuration of basal-to-RE texture or RE-to-C texture have a moderate fracture elongation, ranging from 20% to 30%. While the pure Mg and Mg-Gd binary alloys with the basal texture or C-texture have the lowest fracture elongation, smaller than 20%. Besides, the tensile stress of Mg-Gd binary alloys does not increase linearly with the Gd concentration (Fig. 16(b)). Both the yield stress and ultimate tensile stress exhibit a softening phenomenon with the basal texture transitioning to RE texture owing to the decrease of Schmid factor of basal slip. Due to the grain size and maximum texture intensity of the Mg-Gd binary alloys over a broad Gd-concentration range (from 0.5 wt.% to 12 wt.%) are very similar, the appearance of summit during the evolution of elongation and the valley during the evolution of tensile stress should be closely related with the texture component. Hereinto, the Mg-Gd alloys with the RE texture possess the highest fracture elongation and are the most promising Mg alloys toward high ductility by texture engineering. The excellent fracture elongation of Mg-Gd alloys with the RE texture originate from a larger fraction of grains that are favorably orientated for plastic deformation, and thus improves the strain homogeneity [68].

This work reveals that the extrusion texture of Mg-RE alloy depends not only on the alloying concentration, but also on extrusion parameters. Moreover, it has proved that the mutual transformation between basal texture, RE texture and abnormal C-texture can be achieved either by modifying the alloying concentration or by changing the extrusion variables. Therefore, we believe this work can pave the way for the design of high-performance extruded Mg alloys by texture engineering.

5. Conclusions

This work aims to investigate formation and transformation mechanism of various texture components in Mg alloys using the EBSD measurements aided with the IGMA analysis. The following conclusions can be drawn from this study:

(1) The transformation from the basal fiber texture in pure Mg to RE-texture in dilute Mg-Gd alloy, and final to C-texture in the high-concentration Mg-Gd alloy is a progressive and composition-dependent process and is a result of more and more grains gradually tilt their c-axis to ED with the increase of Gd element.

(2) Discontinuous dynamic recrystallization, which is prevalent in pure Mg, suffers an increasing retardation with the increase of Gd concentration, and thus impedes the development of basal fiber texture in the recrystallized microstructure.

(3) In Mg-Gd alloy, especially with high concentration Gd, nucleation of dynamic recrystallization is highly heterogenous, only occurring within shear bands. Dynamic recrystallization nucleates within shear bands with an initial orientation that is similar with the host deformed grains, and then reoriented by tilting their c-axis to ED along with the nucleuses growth to form either the RE-texture or C-texture depending on the store energy within shear bands.

(4) Shear bands originate from the profuse, but heterogenous activation of pyramidal I slip, which is in favor of the reorientation process of dynamically recrystallized grains, and thereby rationalized the texture transformation mechanism.

(5) The mutual transformation between basal texture, RE texture and abnormal C-texture can be achieved either by modifying the alloying concentration or by changing the extrusion variables. While the fracture elongation of Mg-Gd alloys exhibits a close correlation with texture types. This finding provides a useful guideline towards high-ductility Mg alloys by texture engineering.

Declaration of competing interest

The authors declare that they have no known competing financial interests or personal relationships that could have appeared to influence the work reported in this paper.

CRediT authorship contribution statement

X.Z. Jin: Writing – review & editing, Writing – original draft, Methodology, Investigation, Formal analysis, Data curation. **G.J. Yang:** Writing – review & editing, Validation, Methodology, Investigation, Data curation. **Xinyu Xu:** Writing – review & editing, Methodology, Data curation, Writing – review & editing, Methodology, Data curation. **D.B. Shan:** Supervision, Methodology, Conceptualization. **B. Guo:** Supervision, Methodology, Conceptualization. **B.B. He:** Writing – review & editing, Supervision, Conceptualization. **C. Fan:** Writing – review & editing, Supervision, Conceptualization. **W.C. Xu:** Writing – review & editing, Supervision, Funding acquisition.

Acknowledgments

The research leading to these results has received funding from the National Natural Science Foundation of China under Grant No 52275327.

Supplementary materials

Supplementary material associated with this article can be found, in the online version, at doi:10.1016/j.jma.2024.10.004.

References

[1] D. Raabe, C.C. Tasan, E.A. Olivetti, Nature 575 (2019) 64–74.
[2] M.T. Perez-Prado, C.M. Cepeda-Jiménez, Nature 528 (2015) 486–487.
[3] T.M. Pollock, Science 328 (2010) 986–987.
[4] M.T. Pérez-Prado, J. Bohlen, S. Yi, D. Letzig, T. Al-Samman, J. Robson, M. Barnett, W. Poole, C. Mendis, S. Agnew, N. Stanford, JOM 72 (2020) 2561–2567.
[5] Z. Wu, W.A. Curtin, Nature 526 (2015) 62–67.
[6] D.D. Yin, C.J. Boehlert, L.J. Long, G.H. Huang, H. Zhou, J. Zheng, Q.D. Wang, Int. J. Plast. 136 (2021) 102878.
[7] S.C. Jin, Y.J. Kim, D.H. Lee, S.H. Han, S. Jo, S.H. Park, J. Mater. Sci. Technol. 191 (2024) 233–249.
[8] C.D. Barrett, A. Imandoust, A.L. Oppedal, K. Inal, M.A. Tschopp, H. El Kadiri, Acta Mater 128 (2017) 270–283.
[9] J. Bohlen, M.R. Nürnberg, J.W. Senn, D. Letzig, S.R. Agnew, Acta Mater 55 (2007) 2101–2112.

[10] S.K. Woo, R. Pei, T. Al-Samman, D. Letzig, S. Yi, J. Magnes. Alloy. 10 (2022) 146–159.
[11] Q. Yang, B. Jiang, H. Pan, B. Song, Z. Jiang, J. Dai, L. Wang, F. Pan, J. Magnes. Alloy. 2 (2014) 220–224.
[12] W. Wang, W. Xie, T. Kang, X. Liu, L. Hu, W. Zhang, H. Liu, W. Chen, W. Zhang, S. Zhou, J. Magnes. Alloy. (2024).
[13] Y. Wang, F. Li, Y. Wang, X.M. Xiao, J. Magnes. Alloy. 11 (2023) 684–693.
[14] Q. Peng, X. Hou, L. Wang, Y. Wu, Z. Cao, L. Wang, Mater. Des. 30 (2009) 292–296.
[15] N. Stanford, R.K.W. Marceau, M.R. Barnett, Acta Mater 82 (2015) 447–456.
[16] T. Zhao, Y. Hu, Y. Wang, Y. Dai, T. Zheng, Z. Li, K. Li, B. He, C. Zhang, F. Pan, J. Magnes. Alloy. (2023).
[17] R. Ahmad, Z. Wu, W.A. Curtin, Acta Mater 183 (2020) 228–241.
[18] R. Ahmad, B. Yin, Z. Wu, W.A. Curtin, Acta Mater 172 (2019) 161–184.
[19] Z. Wu, R. Ahmad, B. Yin, S. Sandlöbes and W.A. Curtin, *Science*, 359, 2018, 447-452.
[20] S. Sandlöbes, M. Friák, S. Zaefferer, A. Dick, S. Yi, D. Letzig, Z. Pei, L.F. Zhu, J. Neugebauer, D. Raabe, Acta Mater 60 (2012) 3011–3021.
[21] D. Guan, X. Liu, J. Gao, L. Ma, B.P. Wynne, W.M. Rainforth, Sci. Rep. 9 (2019) 1–11.
[22] D. Guan, W.M. Rainforth, J. Gao, L. Ma, B. Wynne, Acta Mater 145 (2018) 399–412.
[23] V.M. Miller, J.F. Nie, T.M. Pollock, J. Magnes. Alloy. 10 (2022) 3041–3053.
[24] M.G. Jiang, C. Xu, H. Yan, T. Nakata, Z.W. Chen, C.S. Lao, R.S. Chen, S. Kamado, E.H. Han, J. Magnes. Alloy. 9 (2021) 1797–1805.
[25] L.Y. Zhao, H. Yan, R.S. Chen, E.H. Han, J. Magnes. Alloy. 9 (2021) 818–828.
[26] I. Basu, T. Al-Samman, Acta Mater 67 (2014) 116–133.
[27] Q. Ma, B. Li, W.R. Whittington, A.L. Oppedal, P.T. Wang, M.F. Horstemeyer, Acta Mater 67 (2014) 102–115.
[28] J. Wang, M.R.G. Ferdowsi, S.R. Kada, S. Babaniaris, B. Hutchinson, P.A. Lynch, M.R. Barnett, Scr. Mater. 210 (2022) 0–4.
[29] X.Z. Jin, W.C. Xu, D.B. Shan, B. Guo, B. Jin, M.T. Pérez-Prado, J. Magnes. Alloy. 11 (2021) 1656–1671.
[30] X. Jin, W. Xu, Z. Yang, C. Yuan, D. Shan, B. Teng, B.C. Jin, J. Mater. Sci. Technol. 45 (2020) 133–145.
[31] S. Lyu, W. Xiao, G. Li, D. Xia, Y. Huang, S. Gavras, N. Hort, R. Zheng, C. Ma, J. Alloys Compd. 821 (2020) 153477.
[32] A. Imandoust, C.D. Barrett, A.L. Oppedal, W.R. Whittington, Y. Paudel, H. El Kadiri, Acta Mater 138 (2017) 27–41.
[33] C.M. Cepeda-Jiménez, J.M. Molina-Aldareguia, M.T. Pérez-Prado, Acta Mater 88 (2015) 232–244.
[34] I.H. Jung, M. Sanjari, J. Kim, S. Yue, Scr. Mater. 102 (2015) 1–6.
[35] N. Stanford, Mater. Sci. Eng. A. 527 (2010) 2669–2677.
[36] C.M. Cepeda-Jiménez, J.M. Molina-Aldareguia, F. Carreño, M.T. Pérez-Prado, Acta Mater 85 (2015) 1–13.
[37] N.V. Dudamell, I. Ulacia, F. Gálvez, S. Yi, J. Bohlen, D. Letzig, I. Hurtado, M.T. Pérez-Prado, Acta Mater 59 (2011) 6949–6962.
[38] F.X. Lin, C.C. Wu, X.Y. Fang, H. Liu, J.F. Nie, Scr. Mater. 224 (2023) 10–13.
[39] X. Liu, J. Wang, Sci. Rep. 6 (2016) 1–8.
[40] A. Galiyev, R. Kaibyshev, G. Gottstein, Acta Mater 49 (2001) 1199–1207.
[41] K.J. Tam, M.W. Vaughan, L. Shen, M. Knezevic, I. Karaman, G. Proust, Int. J. Plast. 142 (2021) 1–22.
[42] N.G. Ross, M.R. Barnett, A.G. Beer, Mater. Sci. Eng. A. 619 (2014) 238–246.
[43] K. Hantzsche, J. Bohlen, J. Wendt, K.U. Kainer, S.B. Yi, D. Letzig, Scr. Mater. 63 (2010) 725–730.
[44] J.P. Hadorn, K. Hantzsche, S. Yi, J. Bohlen, D. Letzig, S.R. Agnew, Metall. Mater. Trans. A Phys. Metall. Mater. Sci. 43 (2012) 1363–1375.
[45] J.P. Hadorn, K. Hantzsche, S. Yi, J. Bohlen, D. Letzig, J.A. Wollmershauser, S.R. Agnew, Metall. Mater. Trans. A Phys. Metall. Mater. Sci. 43 (2012) 1347–1362.
[46] L.W.F. Mackenzie, M.O. Pekguleryuz, Scr. Mater. 59 (2008) 665–668.
[47] Q. Zhang, T.W. Fan, L. Fu, B.Y. Tang, L.M. Peng, W.J. Ding, Intermetallics 29 (2012) 21–26.
[48] T. Tsuru, D.C. Chrzan, Sci. Rep. 5 (2015) 1–8.
[49] K.D. Molodov, T. Al-Samman, D.A. Molodov, Acta Mater 240 (2022) 118312.
[50] C.D. Barrett, A. Imandoust, H. El Kadiri, Scr. Mater. 146 (2018) 46–50.
[51] R. Pei, Y. Zou, M. Zubair, D. Wei, T. Al-Samman, Acta Mater 233 (2022) 117990.
[52] J. Bai, Z. Xu and L. Qian, *Mater. Des.*, **220**, 2022,110859.
[53] S.V. Harren, H.E. Dève, R.J. Asaro, Acta Metall 36 (1988) 2435–2480.
[54] I.B. Üçel, E. Kapan, O. Türkoğlu, C.C. Aydiner, Int. J. Plast. 118 (2019) 233–251.
[55] E. Dogan, M.W. Vaughan, S.J. Wang, I. Karaman, G. Proust, Acta Mater 89 (2015) 408–422.
[56] S. Sandlöbes, S. Zaefferer, I. Schestakow, S. Yi, R. Gonzalez-Martinez, Acta Mater 59 (2011) 429–439.
[57] S.E. Ion, F.J. Humphreys, S.H. White, Acta Metall 30 (1982) 1909–1919.
[58] Y. Wang, Y. Xin, H. Yu, L. Lv, Q. Liu, J. Alloys Compd. 644 (2015) 147–154.
[59] K. Zhang, J.H. Zheng, Y. Huang, C. Pruncu, J. Jiang, Mater. Des. 193 (2020) 108793.
[60] B.Q. Shi, Y.Z. Wang, X.L. Shang, L.Y. Zhao, C.Q. Li, D.C. Chen, B.H. Nie, R.S. Chen, W. Ke, Mater. Charact. 187 (2022) 111853.
[61] J. Peng, Z. Zhang, Y. Li, W. Zhou, Y. Wu, Mater. Sci. Eng. A. 703 (2017) 244–250.
[62] H. Yan, S.W. Xu, R.S. Chen, S. Kamado, T. Honma, E.H. Han, Scr. Mater. 64 (2011) 141–144.
[63] M.R. Barnett, M.D. Nave, C.J. Bettles, Mater. Sci. Eng. A. 386 (2004) 205–211.
[64] J. Kuang, T.S.E. Low, S.R. Niezgoda, X. Li, Y. Geng, A.A. Luo, G. Tang, Int. J. Plast. 87 (2016) 86–99.
[65] H. Rikihisa, T. Mori, M. Tsushida, H. Kitahara, S. Ando, Mater. Trans. 58 (2017) 1656–1663.
[66] K.Y. Zhu, D. Chaubet, B. Bacroix, F. Brisset, Acta Mater 53 (2005) 5131–5140.
[67] M.A. Steiner, J.J. Bhattacharyya, S.R. Agnew, Acta Mater 95 (2015) 443–455.
[68] Z. Yan, X. Li, J. Zheng, Z. Zhang, Q. Wang, K. Xu, H. Fan, G. Zhang, J. Zhu, Y. Xue, J. Magnes. Alloy. 9 (2021) 964–982.